

1 **Modeling Kelvin Helmholtz Instability Tube & Knot**
2 **Dynamics and Their Impact on Mixing in the Lower**
3 **Thermosphere**

4 **Tyler S. Mixa^{1,2}, Thomas S. Lund², and David C. Fritts^{1,2}**

5 ¹Center for Space and Atmospheric Research (CSAR), Embry-Riddle Aeronautical University
6 ²Global Atmospheric Technologies and Sciences (GATS)-inc Boulder

7 **Key Points:**

- 8 • Tube & knot (T&K) dynamics yield faster, more aggressive instability evolutions
9 than axially uniform KHI in stratified shear environments.
10 • T&K-induced twist waves drive the turbulent transition and preclude secondary
11 CI/KHI that dominate prior laboratory and simulation studies.
12 • T&K-induced turbulence yields faster/larger kinetic energy depletion and entropy
13 production, producing more mixing with weaker efficiency.

Abstract

We present modeling results of Kelvin Helmholtz Instability (KHI) tube and knot (T&K) dynamics accompanying a thermospheric KHI event captured by the 2018 Super Soaker campaign (Mesquita et al., 2020). Chemical tracers released by a rocketsonde on 26 January 2018 showed a coherent KHI in the lower thermosphere that rapidly deteriorated within 45-90 s. Using wind and temperature data from the event, we conducted high resolution direct numerical simulations (DNS) employing both wide and narrow spanwise domains to facilitate (wide domain case) and prohibit (narrow domain case) the axial deformation of KH billows that allows tubes and knots to form. KHI T&K dynamics are shown to produce accelerated instability evolution consistent with the observations, achieving peak dissipation rates nearly 2 times larger and 1.8 buoyancy periods faster than axially uniform KHI generated by the same initial conditions. Rapidly evolving twist waves are revealed to drive the transition to turbulence; their evolution precludes formation of secondary convective instabilities (CI) and secondary KHI seen to dominate the turbulence evolution in artificially constrained laboratory and simulation environments. T&K dynamics extract more kinetic energy from the background environment and yield greater irreversible energy exchange and entropy production, yet they do so with weaker mixing efficiency due to greater energy dissipation. The results suggest that enhanced mixing from thermospheric KHI T&K events could account for the discrepancy between modeled and observed mixing in the lower thermosphere (Liu, 2021; Garcia et al., 2014) and merits further study.

1 Introduction

On 26 January 2018, a Kelvin-Helmholtz Instability (KHI) event was observed at the unusually high altitude of 102 km by a Rocketsonde chemical tracer release over Poker Flats, Alaska (Mesquita et al., 2020). The KH billows had horizontal wavelengths of $\lambda_h = 9.6$ km and rapidly deteriorated from their initial coherent state in a scant 45-90 s, indicating an aggressive underlying shear layer with an approximate half depth of $d \approx \lambda_h/4\pi \approx 800$ m. In-situ Rocketsonde wind profiles revealed an apparent superposition of an inertial gravity wave (GW)-induced shear layer and a smaller-scale shear sheet causing the elevated local shear. Lidar measurements from the Poker Flats Research Range showed a similarly sharp temperature enhancement near the same altitude, yielding a local minimum Richardson number (Ri) of 0.05 consistent with rapid shear turbulence evolution.

Highly localized multi-scale environments comprised of such “sheet and layer” superpositions are found throughout the atmosphere and have been shown to produce instability events yielding widespread turbulence with elevated dissipation (see e.g., Fritts et al., 2017, and citations therein), yet their contributions to larger-scale mixing and chemical constituent distributions remain largely unknown. General circulation models (GCMs) represent mixing with the vertical eddy diffusion coefficient, K_{zz} , which approximates heat fluxes and transport due to gravity wave breaking but does not address mixing contributions from other sources. K_{zz} is estimated by applying linear saturation theory to a GCM’s parameterized gravity wave spectra (Garcia et al., 2007; Liu, 2000); it accounts for turbulence localization with inverse Prandtl number scaling (e.g., Fritts & Dunkerton, 1985; McIntyre, 1989) but otherwise neglects nonlinear dynamics and subgrid-scale turbulence. The resulting mixing estimates yield a near-50% deficit from observations: WACCM profiles of gravity wave-parameterized K_{zz} show values of 5-50 $\text{m}^2 \text{s}^{-1}$ from 80-100 km (Liu, 2021) whereas global mean O density profiles measured by the Scanning Imaging Absorption Spectrometer for Atmospheric Chartography (SCIAMACHY) instrument suggest $K_{zz} \sim 10\text{-}80 \text{ m}^2 \text{ s}^{-1}$ over 80-100 km (Swenson et al., 2018), a factor of 1.6-2x larger.

Weaker mixing in WACCM mischaracterizes the transport and global distributions of CO_2 and other constituents. CO_2 mixing ratios are consistently too small above 100

65 km and do not match the observed falloff with altitude (Garcia et al., 2014). Similarly,
 66 Na and Fe transport are both under-estimated in WACCM; fluxes of Na and Fe need to
 67 be larger to agree with cosmic dust and ablation models (Gardner, 2018). Several efforts
 68 have been made to yield greater mixing in GCMs by incorporating parameterized heat
 69 fluxes from propagating gravity waves (Gardner, 2018) and reducing Pr to produce bet-
 70 ter agreement with observations (Garcia et al., 2014). However, Liu (2021) maintains
 71 that subgrid-scale dynamics in the MLT account for the majority of the modeled mix-
 72 ing deficit.

73 Localized shear turbulence events must be considered as a possible mixing source
 74 in the mesosphere and lower thermosphere (MLT) to address this mixing deficiency in
 75 GCMs. Sharp wind and temperature gradients such as those underlying the Mesquita
 76 event exist throughout the atmosphere at scales below the resolution limit of GCMs, and
 77 the resulting *Ri*-critical shear layers produce local instabilities everywhere they occur.
 78 Such events arise in multi-scale environments exhibiting what are described as “sheet
 79 and layer” structures, which occur throughout the atmosphere into the MLT and which
 80 modeling reveals to be prolific sources of local KHI (Fritts & Wang, 2013; Fritts et al.,
 81 2013), see e.g., Kantha et al. (2017); Doddi et al. (2021); Barat (1982); Sato and Wood-
 82 man (1982); Lehmacher et al. (2011); Mesquita et al. (2020). Though ubiquitous, GCM
 83 resolution cannot capture these dynamics (Fritts, Lund, et al., 2022) and their mixing
 84 contributions remain unaddressed.

85 Recent simulations and observations further suggest that many shear-induced in-
 86 stability events undergo “tube and knot” (T&K) dynamics and could account for more
 87 mixing than previously attributed to these events. The conventional understanding of
 88 KHI evolution assumes billows that are axially uniform, with expected morphologies of
 89 turbulence scale progression driven by secondary convective instabilities (CI) forming
 90 in the billow cores and secondary KHI in the billow braids (see e.g., Klaassen & Peltier,
 91 1985; Peltier & Caulfield, 2003; Fritts et al., 2014). Real shear layers, however, are not
 92 infinitely uniform; variable intensities and depths over their spatial extent will impact
 93 the axial coherence of KHI. Laboratory experiments by Thorpe (1987) showed that even
 94 in an artificially uniform environment, KHI “tubes” and “knots” arise and intensify be-
 95 tween adjacent, misaligned KH billows prior to the evolution of secondary CI and KHI
 96 (see e.g., Fritts et al., 2021a). Over 30 years later, observations by Hecht et al. (2021)
 97 revealed KHI T&K dynamics occurring in the MLT, and subsequent modeling and a re-
 98 view of other MLT observational evidence revealed these dynamics to be widespread, per-
 99 haps even ubiquitous, in the MLT (Fritts et al., 2021a; Fritts, Wang, Lund, & Thorpe,
 100 2022). However, T&K simulations to-date have only occurred in idealized environments
 101 that don’t directly correspond to observed atmospheric conditions. Given the potential
 102 of KHI T&K dynamics to promote elevated mixing in the MLT, it is imperative to in-
 103 vestigate the impact of T&K dynamics on observed shear turbulence events to determine
 104 if they can account for the missing mixing modeled in the MLT.

105 In this study, we evaluate the impact KHI T&K dynamics on the 26 January 2018
 106 thermospheric KHI event reported by Mesquita et al. (2020). In approximating the ob-
 107 served KHI dynamics we demonstrate how T&K formation accelerates and intensifies
 108 billow turbulence evolution to promote enhanced dissipation and mixing. To isolate T&K
 109 influences, identically initialized direct numerical simulations (DNS) of the Mesquita event
 110 are conducted with two spanwise (axial) domain sizes: an 8 KHI λ_h domain allowing T&K
 111 formation and a 0.5 KHI λ_h domain prohibiting axial non-uniformity. T&K formation
 112 is shown to yield rapid proliferation of small-scale turbulent features in places where KH
 113 billows link that both form and dissipate at earlier times than the secondary CI/KHI-
 114 driven turbulence transition of axially uniform KHI. T&K driven dynamics achieve peak
 115 dissipation at twice the speed and amplitude of the equivalent case limited to axially uni-
 116 form KHI, with similarly enhanced and accelerated mixing. The significant impact of
 117 T&K dynamics in this environment suggests extensive contributions to momentum trans-

118 port and deposition that could aid the development of improved mixing parameteriza-
 119 tions in GCMs.

120 The remainder of the paper is organized as follows: Section 2 presents a descrip-
 121 tion of the numerical methods, including the governing equations, solution method, and
 122 simulation parameters employed by our numerical model; the procedure to determine
 123 representative initial conditions from the available observations; and the nondimensional
 124 parameters defining the simulation environment. Simulation results are presented in Sec-
 125 tion 3, evaluating the instability characteristics, dissipation and energy exchange, and
 126 mixing characteristics promoted by T&K dynamics relative to their absence. Section 4
 127 contains the summary and conclusions of our results.

128 2 Numerical Methods

129 2.1 CGCAM Model Architecture

130 Simulations herein are conducted using the Complex Geometry Compressible At-
 131 mosphere Model (CGCAM). CGCAM solves the nonlinear, compressible Navier-Stokes
 132 equations, written in divergence form as:

$$\frac{\partial \rho}{\partial t} + \frac{\partial (\rho u_j)}{\partial x_j} = 0 \quad (1)$$

$$\frac{\partial (\rho u_i)}{\partial t} + \frac{\partial (\rho u_i u_j)}{\partial x_j} = -\frac{\partial p}{\partial x_i} - \rho g \delta_{i3} + \frac{\partial \sigma_{ij}}{\partial x_j} \quad (2)$$

$$\frac{\partial \rho E}{\partial t} + \frac{\partial [(\rho E + p) u_j]}{\partial x_j} = -\rho g u_3 + \frac{\partial (u_i \sigma_{ij})}{\partial x_j} - \frac{\partial q_j}{\partial x_j} \quad (3)$$

133 where σ_{ij} and q_j are the viscous stress and thermal conduction, defined as

$$\sigma_{ij} = \mu \left[\left(\frac{\partial u_i}{\partial x_j} + \frac{\partial u_j}{\partial x_i} \right) - \frac{2}{3} \left(\frac{\partial u_k}{\partial x_k} \right) \delta_{ij} \right] \quad \text{and} \quad q_j = -\kappa \frac{\partial T}{\partial x_j} \quad (4)$$

134 Here μ is the dynamic viscosity, κ is the thermal conductivity, and δ_{ij} is the Kronecker
 135 delta. μ and κ depend on the temperature through Sutherland's Law (White, 1974). The
 136 solution variables are the air density ρ , the momentum per unit volume ρu_i or $(\rho u, \rho v, \rho w)$
 137 with velocity components $(u_i, u_j, u_k) = (u, v, w)$ along (x, y, z) . Energetics and entropy
 138 are discussed in Section 3.3.

139 We assess the evolution of instability features via the vorticity magnitude

$$|\zeta| = |\nabla \times u| \quad (5)$$

140 and the intermediate eigenvalue λ_2 of the tensor

$$\mathcal{H} = \mathcal{S}^2 + \mathcal{R}^2 \quad (6)$$

141 (see e.g., Jeong & Hussain, 1995), where \mathcal{S} and \mathcal{R} are the strain and rotation rate ten-
 142 sors, with components defined as

$$\mathcal{S}_{ij} = \frac{1}{2} \left(\frac{\partial u_i}{\partial x_j} + \frac{\partial u_j}{\partial x_i} \right) \quad \text{and} \quad \mathcal{R}_{ij} = \frac{1}{2} \left(\frac{\partial u_i}{\partial x_j} - \frac{\partial u_j}{\partial x_i} \right) \quad (7)$$

143 $|\zeta|$ and $|\lambda_2 < 0|$ reveal the dominant features with strong rotational tendencies, enabling
 144 the visualization of emerging KHI, T&K, and twist waves as the flow becomes turbu-
 145 lent.

146 Solution variables are stored at the cell centroids and fluxes on the faces are con-
 147 structed using a kinetic energy-conserving interpolation scheme similar to that discussed
 148 in Felten and Lund (2006) for the incompressible Navier-Stokes equations. The govern-
 149 ing equations are discretized using the finite-volume framework, in which each compu-
 150 tational cell is considered to be a small control volume. The resulting scheme is glob-
 151 ally conservative for mass, momentum, total energy, and kinetic energy. Time advance-
 152 ment is achieved via a low-storage, third-order accurate Runge-Kutta scheme with a vari-
 153 able time step satisfying the CFL stability condition. Additional details for CGCAM are
 154 provided by Dong et al. (2020) and Lund et al. (2020).

155 The model domains employed in these simulations extend 40 km in the streamwise
 156 (x) direction ($4 \text{ KHI } \lambda_h$) and from 90 to 115 km in altitude (z). To enable direct com-
 157 parisons of cases with and without T&K dynamics, DNS were conducted with two span-
 158 wise (y, axial) domain sizes: an 80 km ($8 \text{ KHI } \lambda_h$) domain allowing T&K formation and
 159 a 5 km ($0.5 \text{ KHI } \lambda_h$) domain prohibiting axial non-uniformity. The domain employs pe-
 160 riodic horizontal boundary conditions and characteristic vertical boundary conditions.
 161 2.5 km sponge layers at the top and bottom of the vertical domain constrain the use-
 162 able domain to $92.5 < z < 112.5$ km. Each simulation is executed on Department of
 163 Defense high-performance supercomputers with a $(N_x, N_{y1}, N_{y2}, N_z) = (1824, 3648, 228, 1152)$
 164 grid, having streamwise and spanwise grid resolution of $(\Delta x, \Delta y) = 21.9298$ m and $\Delta z =$
 165 21.7014 m. To seed the instability formation, a white noise spectrum is added to the ini-
 166 tial background wind field with a root mean square amplitude of 10^{-3} m s^{-1} .

167 2.2 Defining Representative Initial Conditions

168 The observational datasets capturing the Mesquita et al. (2020) KHI event include
 169 wind profiles triangulated from the Rocketsonde TMA chemical release, temperature pro-
 170 files from the nearby Poker Flats Na lidar, and remote imaging of the Rocketsonde chem-
 171 ical tracer release revealing the KHI evolution. Raw profiles from the Rocketsonde and
 172 Na lidar (blue curves) and profile decompositions (orange and yellow curves) are shown
 173 in Figure 1, and the modified initial conditions for the simulations are shown in Figure 2.
 174 Rocketsonde zonal and meridional wind profiles (Figure 1a-b) display rotary tendencies
 175 indicating an inertial gravity wave (IGW) with a compressed phase structure generat-
 176 ing a narrow region of enhanced local shear near 103 km. Sinusoidal decomposition of
 177 the winds (Figure 1a-b) reveal a local 4 km λ_z sinusoidal enhancement (orange curves)
 178 superposed with the background 16 km λ_z IGW (yellow curves) underlying the peak shear.
 179 The nearby Na lidar temperature profile (Figure 1c) shows local maximum at 101 km
 180 indicating peak stability 1-2 km lower than the peak shear altitude in the Rocketsonde
 181 winds. The temperature profile is spatially offset from the Rocketsonde measurement
 182 but roughly coincident in time. Lidar data indicates significant temporal variability, with
 183 peak T shifting ± 20 K and ± 2 km in the hour surrounding the event. The dashed line
 184 at the top of the profile indicates a region where a low signal to noise ratio could com-
 185 promise the accuracy of the measured lapse rate. However, lapse rates from the NRLM-
 186 SISE/00 empirical model employed by Mesquita et al. (2020) conservatively estimate a
 187 minimum Richardson number of 0.05 near the KHI altitude.

188 KHI revealed by the chemical tracer exhibit $\lambda_h = 9.6$ km and rapidly deteriorate
 189 in 45-90 s. The underlying layer depth of $d \approx \lambda_h/4\pi = 800$ m that sourced these KHI
 190 is larger than the layer depth in the measured background profiles, suggesting that the
 191 initial layers were deeper and higher in amplitude before the KHI began eroding the layer.
 192 Suitable layer characteristics to excite these KHI require collocated shear and stability
 193 layers of equal characteristic scales with amplitudes that yield the underlying Ri . Given
 194 both the altitude offset between wind and temperature layers and the layer depth dis-
 195 agreement between the measured profiles and the observed KHI, a set of composite pro-
 196 files needs to be generated from the observations to match the KHI event characteris-
 197 tics.

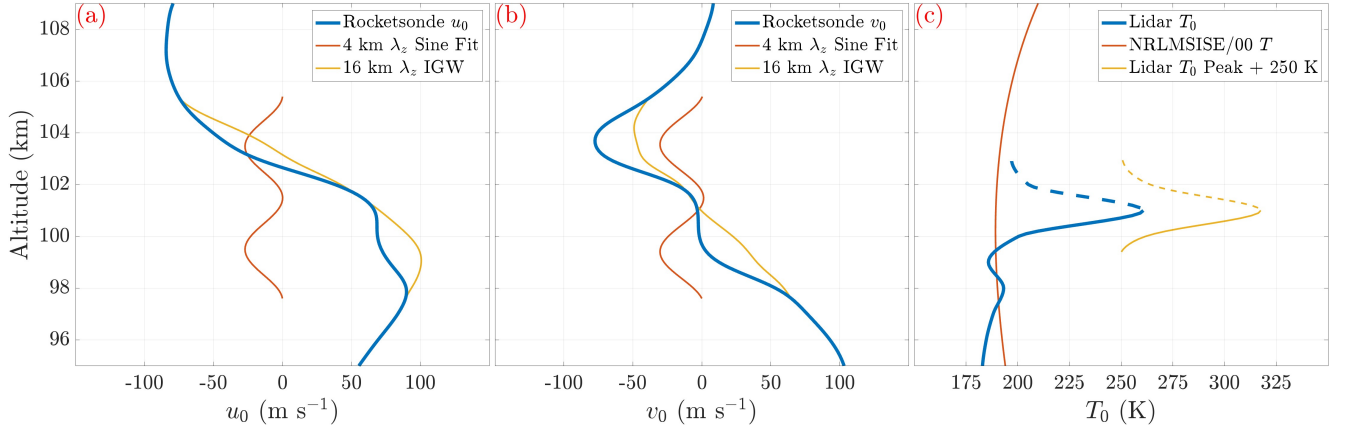


Figure 1. Rocketsonde and Lidar profiles (blue curves) and decompositions (orange and yellow curves) from the Mesquita et al. (2020) KHI event.

198 When working with non-located datasets with different sensitivity to feature evo-
 199 lution, the features of each dataset must be combined in a self-consistent manner that
 200 faithfully represents the underlying environmental parameters dictating the event. Ad-
 201 hering to this approach, input wind and temperature profiles were adapted to comprise
 202 collocated layers that yield Ri and KHI λ_h characteristics matching the observed insta-
 203 bility evolution: (1) An NRLMSISE/00 empirical temperature profile (Figure 1c, orange
 204 curve) was subtracted from T_0 to isolate the temperature peak in the lidar data (Fig-
 205 ure 1c, yellow curve) corresponding to the sinusoidal local wind enhancement. (2) The
 206 lidar temperature peak was then superposed on the model temperature profile at the al-
 207 titude of peak shear to collocate the layers underlying the KHI. (3) The vertical depths
 208 of the temperature peak and 4 km λ_z sinusoidal wind feature were then increased to pro-
 209 duce 800 m shear and stability layers matching the observed KHI, and the peak wind/temperature
 210 amplitudes were increased/decreased to yield a minimum Richardson number of $Ri =$
 211 0.05. (4) To retain the initial background characteristics above the layer, wind/temperature
 212 profiles above their modified peaks were extended vertically with the same vertical shear
 213 ($\partial\{u_0, v_0\}/\partial z$) and stability (N^2) found above the initial layers. (5) For numerical con-
 214 venience, the final wind components were rotated 45° to have maximum shear in the stream-
 215 wise (x) direction at the layer, and the spanwise (y) component of the rotated winds hav-
 216 ing minimum shear was set to 0 m s⁻¹ to prevent spanwise feature advection. Figure 2
 217 shows the measured wind and stability profiles in the rotated domain ($\tilde{u}_0, \tilde{v}_0, N_0^2$) and
 218 the resulting modified profiles ($u_{\text{final}}, v_{\text{final}}, N_{\text{final}}^2$) used to initialize CGCAM runs, where
 219 u and v are the wind components in the x (streamwise) and y (spanwise) coordinate di-
 220 rections of the simulation domain.

221 2.3 Derived Layer and Nondimensional Parameters

222 The layer characteristics of the background profiles are shown in Figure 3, includ-
 223 ing $(\frac{\partial U}{\partial z})^2$, N^2 , and Ri . Shear and stability profiles for the collocated layers are shown
 224 in Figure 3a-b, with 800 m scaled sech^2 and sech^4 profiles (dashed lines) confirming the
 225 layer half depth of the input profiles. The Richardson number is given by

$$226 Ri = N^2 / \left(\frac{\partial U}{\partial z} \right)^2 \quad (8)$$

226 and shown in Figure 3c. The minimum value of $Ri = 0.05$ occurs at the layer center
 227 at 102.9 km.

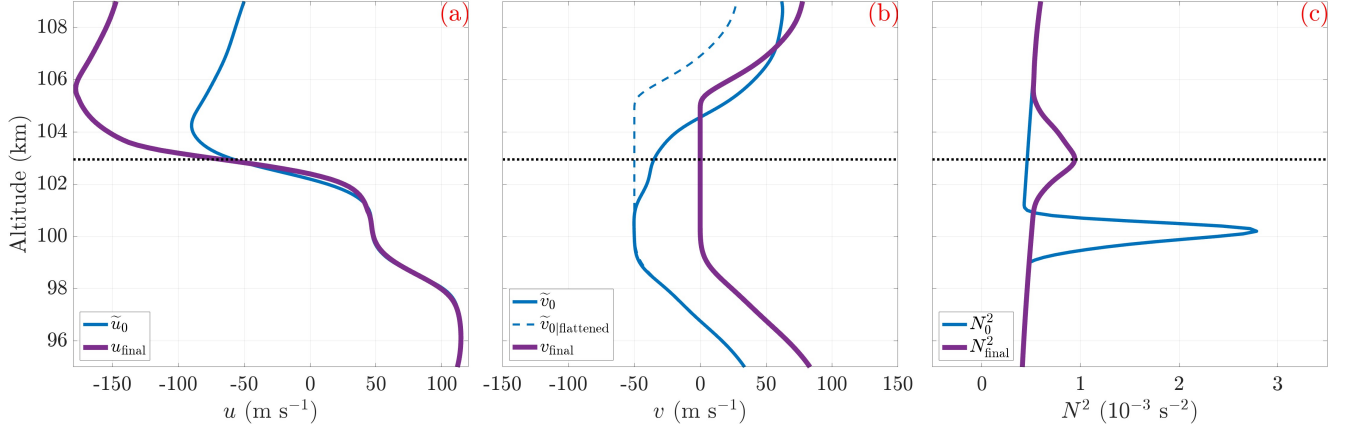


Figure 2. Original and modified background profiles of u , v , and N used to initialize the simulations. Variables are plotted in the rotated coordinate frame of the simulation domain.

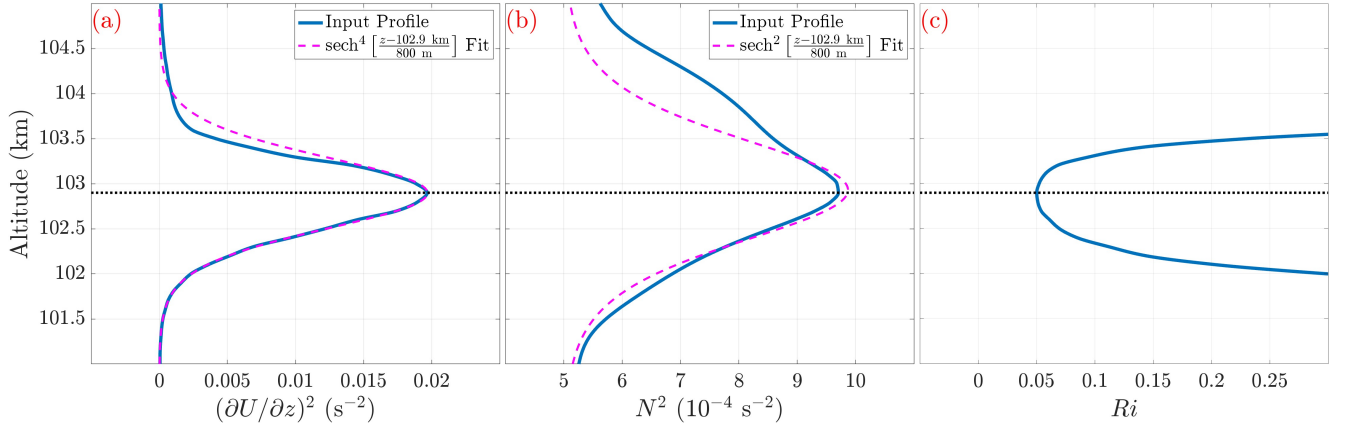


Figure 3. Profiles of the vertical shear $(\frac{\partial U}{\partial z})^2$, stability N^2 , Richardson number Ri , and their associated 800 m fits.

228

The Reynolds number is calculated from the shear layer half depth d as

$$Re = \frac{\rho d \Delta U / 2}{\mu} \quad , \quad (9)$$

229

where ΔU is the velocity difference over the shear layer and μ is the kinematic viscosity. μ is calculated via Sutherlands Law (White, 1974) from the ground reference value $\mu_0 = 1.506 \times 10^{-5} \text{ m}^2 \text{ s}^{-1}$ and the background temperature and density. Peak values of $Re = 2200$ at the layer support the formation of both secondary CI and secondary KHI for this low Ri .

234

Simulations indicated peak horizontally-averaged kinetic energy dissipation rates per unit mass of $\epsilon_m = 2\text{-}3 \text{ W kg}^{-1}$ and a corresponding Kolmogorov length scale of

235

$$\eta = (\nu^3 / \epsilon_m)^{\frac{1}{4}} \approx 12 \text{ m} \quad . \quad (10)$$

236

The domain grid spacing of $\Delta \mathbf{x} \approx 22 \text{ m}$ results in a resolution ratio of $R = \Delta \mathbf{x} / \eta = 1.83$ which satisfies the DNS criteria of $R \approx 1.5\text{-}2.1$ (Moin & Mahesh, 1998; Pope, 2000).

237

Hence, true DNS is achieved and no subgrid-scale turbulence parameterization is required.

238

3 Results

The purpose of the numerical results is to demonstrate how T&K features follow distinct instability pathways that evolve faster, dissipate more energy, and yield more mixing than axially uniform KHI. Section 3.1 presents the instability morphologies of the T&K-allowing DNS, showing how misaligned billow junctions and axial non-uniformity lead to T&K feature superpositions that quickly become turbulent and engulf the domain. Section 3.2 identifies the equivalent instability evolutions in a smaller horizontal domain consistent with previous KHI DNS, where the narrower spanwise dimension precludes axial billow deformations that would otherwise enable T&K dynamics. Here the turbulence is dominated by characteristic secondary CI/KHI and billow pairing as seen in previous studies, dynamics that are precluded by the rapid evolution of T&K-induced dissipation in the wider domain DNS. Section 3.3 compares the dominant dissipation, entropy, and energy exchange metrics in both DNS, demonstrating how both instantaneous and integrated metrics mirror the dominant instability features and yield larger values for the T&K case. Section 3.4 introduces and evaluates the mixing efficiency of both events using a several standard metrics, showing how T&K dynamics produce more mixing but do so at weaker assessed efficiencies.

3.1 Instability Differentiation with T&K

Horizontal overviews (Figure 4) of the vorticity magnitude $|\zeta|$ and intermediate eigenvalue λ_2 in the T&K-allowing DNS reveal spanwise KH billow deformation sites exciting T&K evolutions and twist waves. The horizontal domain is presented in a parallelogram orientation, shifting the center location of the periodic streamwise domain from $x = 0$ km to $x = \pm 20$ km along the spanwise extent of the domain. This display format retains the full extent of the x-y domain in a single plot while elucidating the relative locations of vorticity features straddling the streamwise boundaries. Along the spanwise axis, initial KH billows in panel 1 exhibit local variations in $|\zeta|$ orientation leading to lateral junctions where adjacent billows are misaligned. These distorted billow regions form characteristic T&K structures consistent with (Fritts, Wang, Lund, & Thorpe, 2022; Fritts, Wang, Thorpe, & Lund, 2022) that locally elevate $|\zeta|$:

1. horizontally rotated KH billows produce “billow linking” vortex tubes connecting pairs of streamwise-adjacent billows at marked locations T1-T6; and
2. regions where 2 billows link to 1 (2:1) produce “billow merging” vortex knots in a loop connecting the three spanwise-adjacent billows at marked locations K1-K4.

Each site identified in panel 2 hosts a unique superposition of T&K features connecting up to 5 adjacent KH billows:

- Sites S1 and S5 have a vortex knot with a vortex tube linking one leg of the knot to the adjacent billow at larger x ;
- Site S2 has a vortex knot with a vortex tube linking one leg to the adjacent upstream billow and another vortex tube linking the knot core to the adjacent downstream billow;
- Site S3 has two vortex tubes linking the central billow to both the upstream and downstream billows; and
- Site S4 has a vortex knot with a vortex tube shared with S3 linking the knot core to the adjacent upstream billow.

All five T&K superposition sites break down the parent vortices into mode 1 and mode 2 Kelvin vortex waves referred to here as twist waves (Kelvin, 1880), instability structures comprising radial displacements that rotate along the vortex axis as they propagate away from the initial location. Mode 1 twist waves start with a single radial dis-

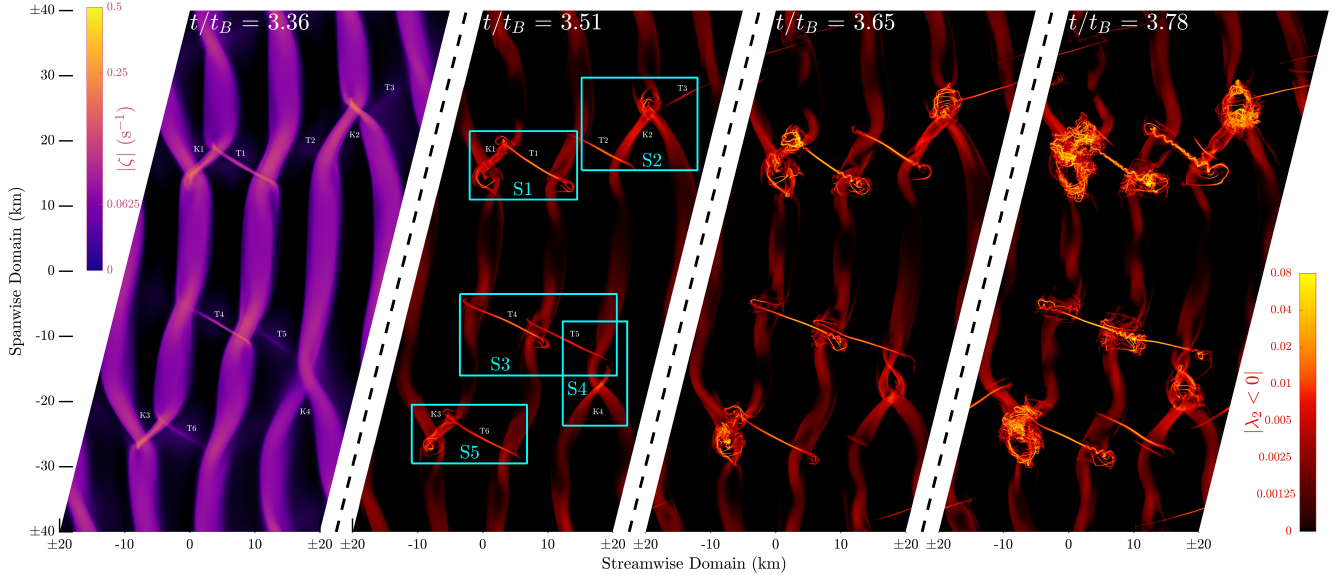


Figure 4. Horizontal cross-sections of the vorticity magnitude (ζ , left) and rotational vorticity component (λ_2 , right panels) showing T&K evolution from 3.36-3.78 t_B . Labeled features are described in the text. See video in supplemental materials for additional times.

287 placement that distorts a cylindrical vortex filament into a helix as it propagates, and
 288 mode 2 twist waves split the vortex filament with a pair of radial displacements that dif-
 289 ferentially advect each other to form a double helix. Panels 2-4 of Figure 4 exhibit sev-
 290 eral characteristic twist wave evolutions for similar sets of T&K feature superpositions.
 291 Billow linking vortex tubes (T1-T6) produce pairs of mode 1 twist waves that propagate
 292 from the linked billows toward the tube centers in panels 3-4. Billow merging vortex knots
 293 having one leg linked to an adjacent billow at Sites S1, S2, and S5 form mode 2 twist
 294 waves in the linked leg of the knot (intersection K1-T1 at S1 and intersection K3-T6 at
 295 S5 in panels 2-4; intersection T2-K2 at S2 in panels 3-4) Larger mode 2 twist waves also
 296 form at Sites S2 and S4 on the single-leg side of 2:1 knots K2 and K4. Knot cores (K1-
 297 K4) also exhibit fragmentation as small scale, adjacent vortices become intertwined. All
 298 of these processes yield finer scale, higher amplitude vorticity structures that drive the
 299 transition to turbulence.

300 Instability sites produced by T&K dynamics generate local, rapidly expanding turbu-
 301 lence regions that quickly engulf the entire horizontal extent of the shear layer. Fig-
 302 ure 5 shows horizontal overviews of the event in the manner of Figure 4 demonstrating
 303 the evolution of widespread turbulence from the initial T&K sites (a full video can be
 304 found in the supplemental materials). Initial billow distortions in panel 1 quickly develop
 305 T&K features that develop mode 1 and mode 2 twist waves (panel 2). Mode 2 twist waves
 306 and the interaction of mode 1 twist wave with adjacent, orthogonal KHI cause fragmen-
 307 tation of KH billow cores. Twist wave-induced fragmentation yields smaller scale, inten-
 308 sified vortical structures, and successive like interactions drive the transition to turbu-
 309 lence as they proliferate in all directions from their source sites (panel 3). Losing their
 310 initial anisotropy, regions of intense turbulence merge and entrain most of the shear layer
 311 into large, well-mixed regions. Turbulence regions promoted by T&K dynamics are no-
 312 tably more aggressive than streamwise swaths of near-axial uniformity at $y = 0$ and
 313 $y = \pm 40$ km, suggesting that T&K dynamics yield more vigorous and intensified tur-
 314 bulence than KHI events constrained to be axially uniform. The evolutions and linkages

315 that lead to intensified T&K dynamics appear to preclude the potential for secondary
 316 CI seen in the axially uniform KHI at later times.

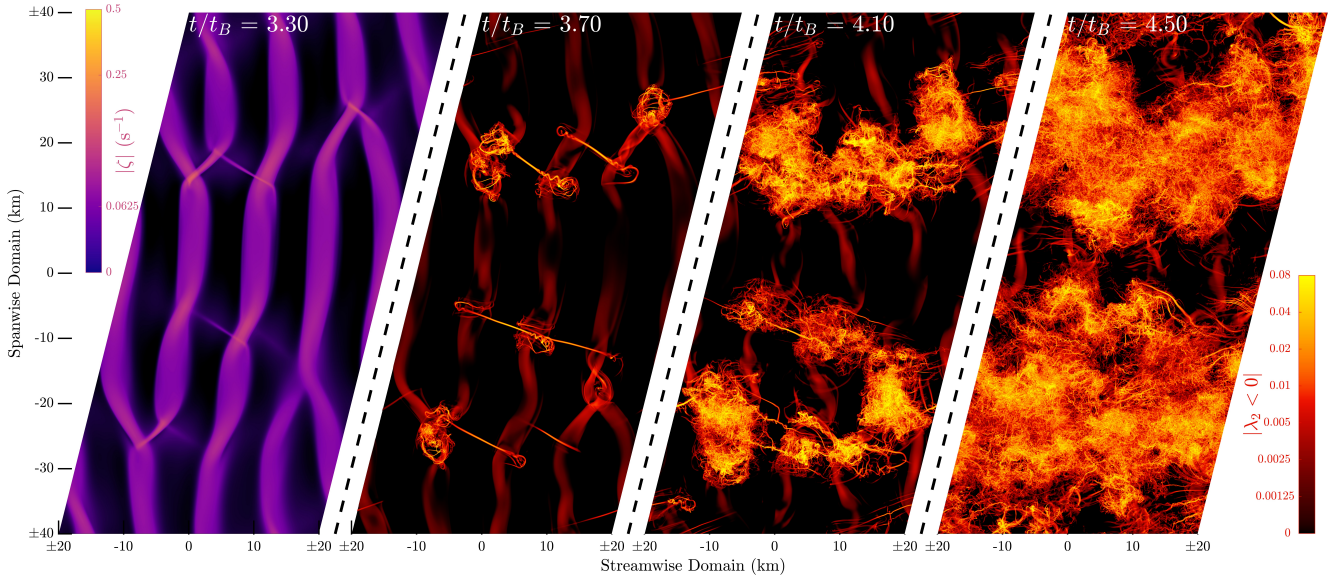


Figure 5. As in Figure 4 for 3.30-4.50 t_B .

3.2 Instability Evolution in Axially Uniform KHI

317

318 Comparing KHI cross sections from the T&K-allowing DNS with the T&K-prohibiting
 319 DNS conclusively shows the radical departures of T&K evolutions from equivalently ini-
 320 tialized, axially uniform KHI. Streamwise-vertical slices (Figure 6a-d) of the tempera-
 321 ture perturbations (T') at $y = 20$ km in the T&K-allowing DNS reveal the following
 322 crucial deviations from domain center T' slices in the T&K-prohibiting DNS (Figure 6e-
 323 h) at the same times:

324

- 325 1. Though initial KHI in both cases (Figure 6a,e) evolve at similar times and scales,
 326 KHI in the T&K-allowing cross-section develop secondary instability structures
 (Figure 6b) while the T&K-prohibiting KHI remain coherent (Figure 6f).
- 327 2. At the latter two times (Figure 6c-d and g-h), the T&K-allowing case is already
 328 well-mixed by the time the T&K-prohibiting case shows signs of weak tertiary in-
 329 stability structures in the periphery of the billow cores.

330

331 w' and T' cross-sections of the T&K-prohibiting DNS in Figure 7 reveal billow merg-
 332 ing that delays secondary CI/KHI formation and elicits stirring oscillations within the
 333 billow cores. Billow merging at $4.76 t_B$ (Figure 7b,f) reduces the number of KHI billows
 334 in the streamwise domain from 4 to 3. As the two central billows merge, their pertur-
 335 bation amplitudes weaken relative to earlier times (Figure 7a,e), further delaying insta-
 336 bility onset. Spanwise cross-sections at $z = 103$ km show no indications of secondary
 337 CI formation until after $4.76 t_B$ (Figure 7i-l), long after turbulence has fully engulfed the
 338 T&K-allowing domain in Figure 6. Prominent secondary KHI form at the top of the bil-
 339 lows at $5.61 t_B$ (Figure 7d,h), driving the transition to turbulence a full $2 t_B$ after the
 340 initial billow formation. Within the billows, peak amplitude regions of T' (w') in the bil-
 341 low core advect horizontally (vertically) about the vertical (horizontal) billow core axis
 342 rather than immediately dissipating. These oscillatory motions delay the fully mixed state
 of horizontal homogeneity to much later times as the entrained fluid stirs about the bil-

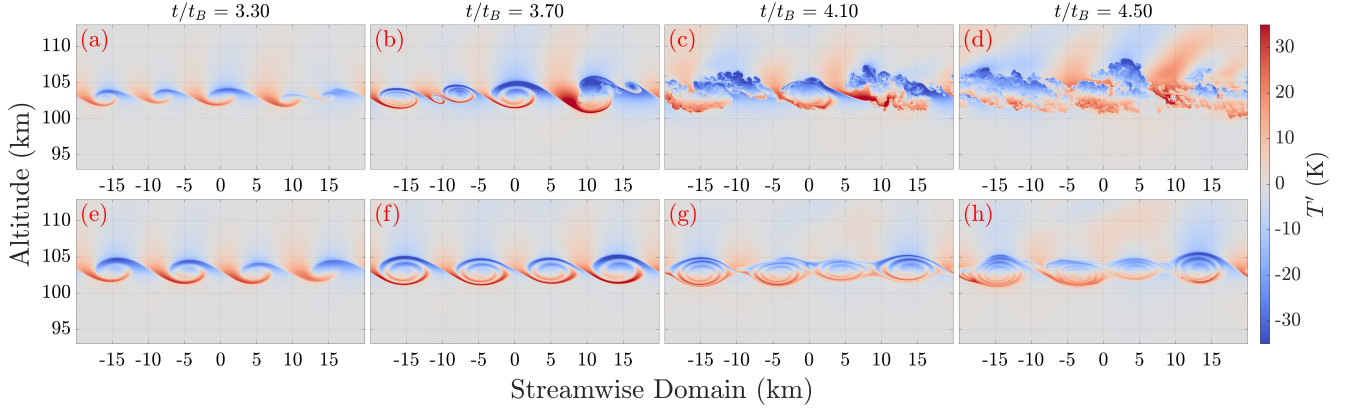


Figure 6. Vertical cross-sections of the temperature perturbation (T') fields comparing KHI evolution in the T&K-allowing (top) and T&K-prohibiting (bottom) DNS results. Times correspond to the four panels in Figure 5.

343 low core for several buoyancy periods (a full video can be found in the supplemental ma-
 344 terials).

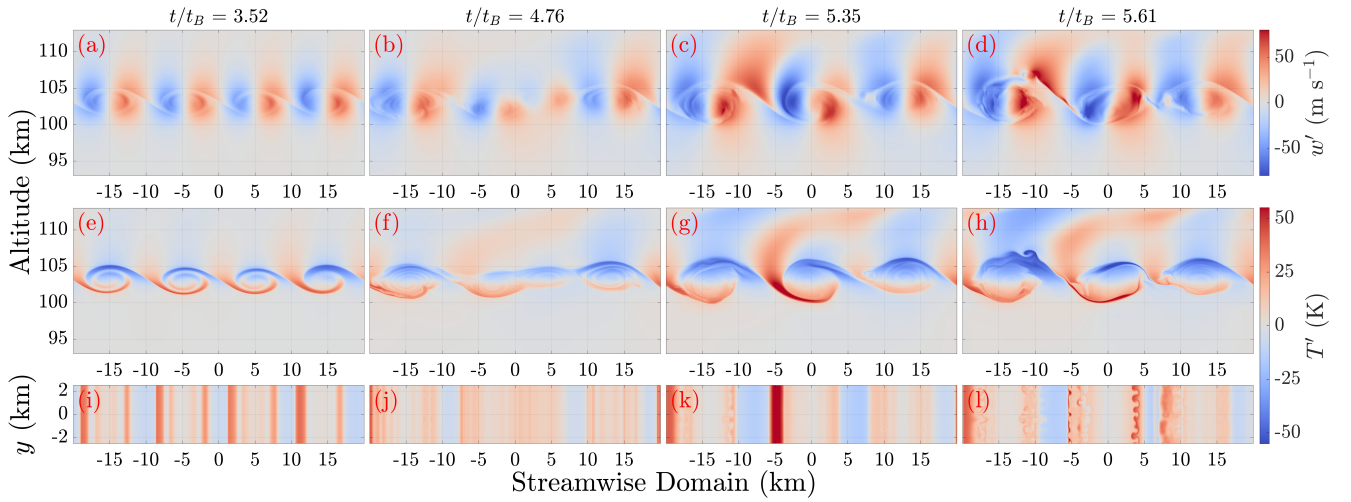


Figure 7. Vertical w' cross-sections (top), vertical T' cross-sections (middle), and horizontal T' cross-sections (bottom) in the T&K-prohibiting DNS results.

345 **3.3 Dissipation and Energy Exchange Differentiation with T&K**

346 To evaluate turbulence and mixing characteristics, we compare the dominant terms
 347 of entropy creation and energetic exchange in the two DNS cases. The production of volume-
 348 averaged entropy, neglecting boundary fluxes, is given by

$$\Delta S = \int \left(\left\langle \frac{\epsilon}{T} \right\rangle + \left\langle \frac{\chi}{T^2} \right\rangle \right) dt \quad , \quad (11)$$

349 where $\epsilon = \sigma_{ij} \mathcal{S}_{ij}$ is the kinetic energy dissipation rate, $\chi = k \left(\frac{\partial T}{\partial x_k} \frac{\partial T}{\partial x_k} \right)$ is the ther-
 350 mal energy dissipation rate, and $\langle \rangle$ indicates volume averaging. $\mathcal{E} = \langle \epsilon \rangle$ is a marker for

351 the onset of 3D turbulence, while $\mathcal{X} = \langle \chi \rangle$ is an approximate metric for perturbation
 352 amplitude growth in the dominant instabilities. The volume-averaged total energy is given
 353 by

$$E = KE + PE + IE \quad , \quad (12)$$

354 where $KE = \langle \rho u_k u_k / 2 \rangle$ is the volume-averaged kinetic energy, $PE = \langle \rho g z \rangle$ is the volume-
 355 averaged potential energy, $IE = c_v \langle T \rangle$ is the volume-averaged internal energy, and c_v
 356 is the specific heat at constant volume. We also assess mixing via energy exchange from
 357 kinetic energy to potential and internal energy:

$$\Delta KE|_{KE \leftrightarrow PE} = \int \mathcal{W}_b dt \quad , \quad (13)$$

358 where $\mathcal{W}_b = \langle \rho g w' \rangle$ is the volume-averaged buoyancy work, and

$$\Delta KE|_{KE \leftrightarrow IE} = \int (\mathcal{E} - \mathcal{W}_{pv}) dt \quad , \quad (14)$$

359 where $\mathcal{W}_{pv} = \left\langle p \frac{\partial u_k}{\partial x_k} \right\rangle$ is the volume-averaged pressure-volume work. Here we note that
 360 of the energy exchange quantities, only \mathcal{E} represents a positive-definite, irreversible (\rightarrow)
 361 depletion of KE ; \mathcal{W}_b and \mathcal{W}_{pv} both constitute bidirectional energy exchange (\leftrightarrow), but
 362 their final equilibrium states (\rightleftharpoons) can be assessed as irreversible work once turbulence
 363 subsides.

364 Figure 8 shows the time evolution of \mathcal{E} , \mathcal{X} , and \mathcal{W}_b for both DNS. Faster instabil-
 365 ity evolution in the T&K-allowing case yields more vigorous dissipation: T&K-driven
 366 turbulence achieves a peak dissipation rate of $\mathcal{E} = 4.95 \times 10^{-7} \text{ W m}^{-3}$ at $4.91 t_B$, 94%
 367 larger and $1.8 t_B$ earlier than the secondary CI/KHI-driven turbulence in the T&K-prohibiting
 368 DNS ($\mathcal{E} = 2.55 \times 10^{-7} \text{ W m}^{-3}$ at $6.68 t_B$). These results expand on the dissipation
 369 analysis of Fritts, Wang, Lund, and Thorpe (2022); Fritts, Wang, Thorpe, and Lund (2022)
 370 and definitively disprove the long-held notion that secondary CI are the primary trig-
 371 ger of enhanced dissipation in stratified shear environments (see e.g., Klaassen & Peltier,
 372 1985; Caulfield & Kerswell, 2000; Peltier & Caulfield, 2003, and citations therein). \mathcal{X} evo-
 373 lutions identify rapid instability amplitude growth accompanying the \mathcal{E} peak in the T&K-
 374 allowing DNS, but \mathcal{X} in the T&K-prohibiting DNS is markedly different, decreasing af-
 375 ter its initial increase at $\sim 3 t_B$ until the onset of elevated \mathcal{E} at $\sim 6 t_B$. The decrease
 376 is correlated with the billow merging identified in Figure 7, showing how merging and
 377 slower secondary CI/KHI growth delay dissipation to later times in the absence of T&K
 378 dynamics. \mathcal{W}_b in the T&K-allowing DNS is predominantly positive, but it is dwarfed by
 379 the periodic positive and negative oscillations in the T&K-prohibiting DNS after $5 t_B$.
 380 These \mathcal{W}_b oscillations correspond to stirring motions identified in Figure 7 (panels c-d;
 381 g-h) for the T&K-prohibiting DNS; though the oscillations have higher absolute ampli-
 382 tudes than in the T&K-allowing DNS, a significant portion of \mathcal{W}_b in the T&K-prohibiting
 383 DNS is reversible and does not contribute to the net mixing in the final state of the flow.

384 Accumulated mixing parameters in Figure 9 show markedly higher event-level dis-
 385 sipation, entropy production, and kinetic energy conversion enabled by T&K dynamics.
 386 Comparable final states are identified by equivalent \mathcal{E} values, where the T&K-allowing
 387 DNS produces 33% larger accumulated \mathcal{E} , 12% larger accumulated \mathcal{X} , and 30% larger
 388 ΔS than the T&K-prohibiting DNS. ΔKE is also 19% larger in the T&K-allowing DNS,
 389 driven primarily by larger and faster \mathcal{E} growth. The partitioned KE exchanges (last two
 390 panels) are both non-monotonic, indicating reversible exchanges via positive \mathcal{W}_{pv} and
 391 negative \mathcal{W}_b . Time evolution of the $KE \leftrightarrow IE$ energy exchange shows an initial KE
 392 increase in both cases (negative values) due to elevated \mathcal{W}_{pv} during the initial KHI rollup.
 393 The duration and amplitude of $IE \Rightarrow KE$ are larger in the T&K-prohibiting DNS
 394 due to the longer duration of KHI billow coherence, but both cases eventually produce
 395 net $KE \rightarrow IE$ after the onset of turbulence. The $KE \leftrightarrow PE$ exchange confirms that
 396 much of the \mathcal{W}_b in the T&K-prohibiting case after $5 t_B$ is reversible; though it achieves

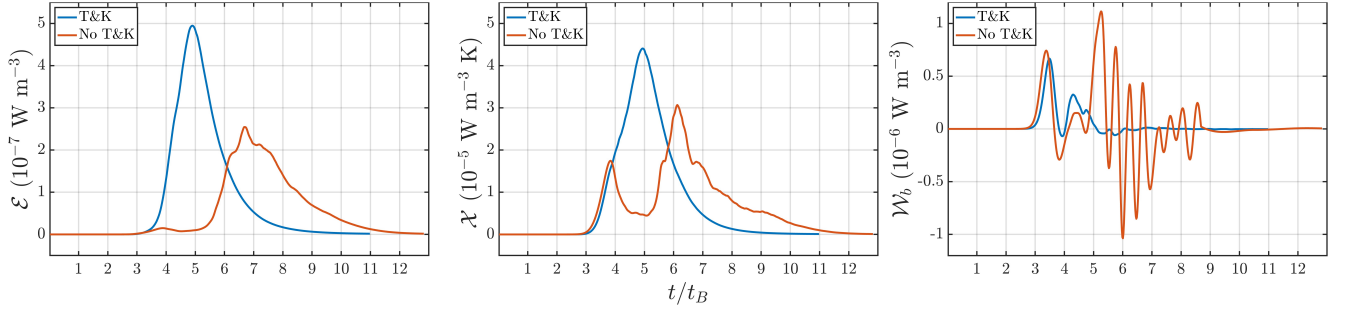


Figure 8. Instantaneous domain-averaged mixing parameters for the T&K-allowing and T&K-prohibiting DNS.

397
398
399

a larger accumulated $KE \Rightarrow PE$ at $6 t_B$, the final $KE \rightleftharpoons PE$ state restores the stirred energy back to KE , producing a $KE \rightarrow PE$ deficit of 4% relative to the T&K-allowing case. The mixing implications of these results are discussed below.

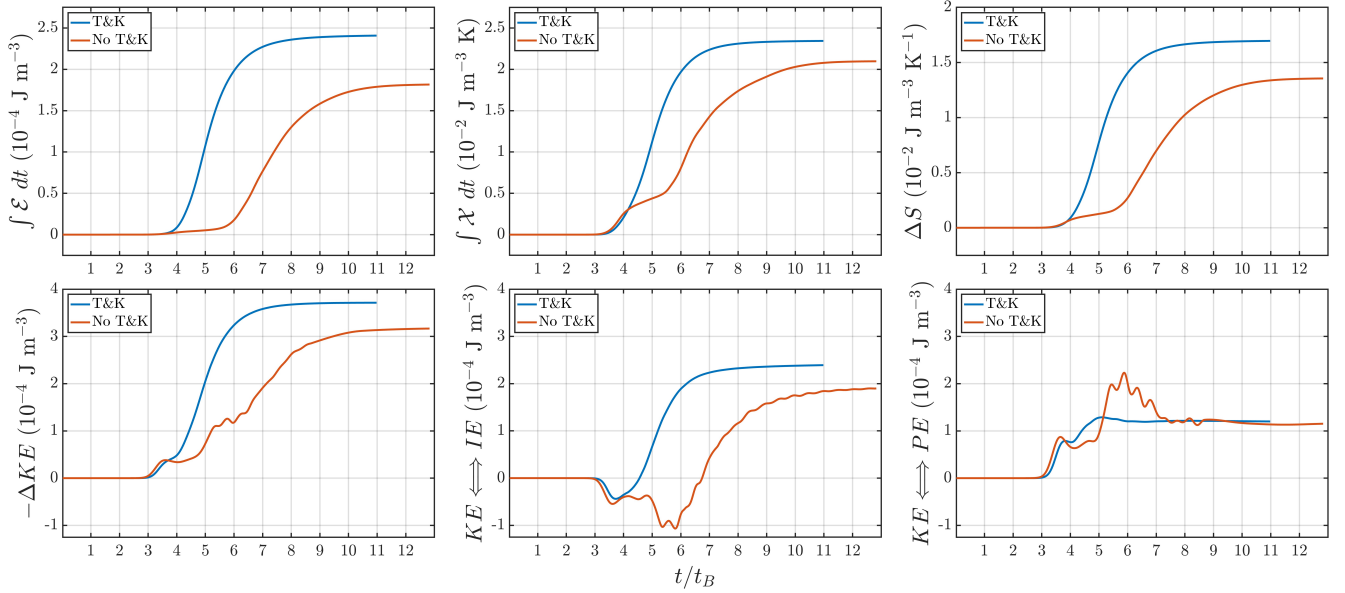


Figure 9. Integrated domain-averaged mixing parameters for the T&K-allowing and T&K-prohibiting DNS, including the resulting ΔS , ΔKE , and the partitioned KE exchanges with IE and PE .

400

3.4 Mixing Efficiency Differentiation with T&K

401
402
403

Broadly, the mixing efficiency γ of a turbulence event is assessed as a ratio of the increase in potential energy to the expended kinetic energy in the final equilibrium state, i.e.

$$\gamma_E = \frac{\Delta PE}{-\Delta KE} \quad (15)$$

404
405
406

(Gregg et al., 2018). Though K_{zz} is useful as an aggregate atmospheric measure in GCMs, γ is the more suitable tool for assessing DNS and can be estimated with K_{zz} from GCMs or observations via the equilibrium assumption methods of T. R. Osborn and Cox (1972)

407 or those of Weinstock (1978); T. Osborn (1980). Equation 15 is often simplified to

$$\gamma_{\mathcal{W}} = \frac{\int \mathcal{W}_b dt}{\int \mathcal{E} dt} \quad (16)$$

408 with the similarly derived flux Richardson number R_f expressed as

$$R_{f|\mathcal{W}} = \frac{\int \mathcal{W}_b dt}{\int (\mathcal{W}_b + \mathcal{E}) dt} \quad (17)$$

409 to be bounded by 1. In Boussinesq flows, Equations 16 and 17 represent the net energy
410 exchanges $KE \rightleftharpoons PE$ and $KE \rightleftharpoons IE$ in the final equilibrium state. The equivalent
411 expressions for a compressible environment are then

$$\gamma_{KE} = \frac{\int \mathcal{W}_b dt}{\int (\mathcal{E} - \mathcal{W}_{pv}) dt} \quad \text{and} \quad R_{f|KE} = \frac{\int \mathcal{W}_b dt}{\int (\mathcal{W}_b + \mathcal{E} - \mathcal{W}_{pv}) dt} \quad (18)$$

412 utilizing the ΔKE partition in Equations 13-14. Winters et al. (1995) proposed the al-
413 ternate metric of available potential energy

$$APE = \rho g(z - z_*) \quad (19)$$

414 to isolate the irreversible mixing at the end state of $KE \rightleftharpoons PE$ in Boussinesq flows,
415 representing the potential energy released when a disturbed density profile adiabatically
416 returns to a monotonically decreasing (z_*) state. Tailleux (2009, 2013) later showed that
417 the volume-averaged net dissipation of APE can be expressed in compressible flows as
418 the time average

$$\overline{D}_{APE} = \overline{\mathcal{W}_b} - \overline{\mathcal{W}_{pv}} \quad (20)$$

419 over the duration of the event. The resulting mixing parameters are given by

$$\gamma_{APE} = \frac{\overline{D}_{APE}}{\overline{\mathcal{E}}} \quad \text{and} \quad R_{f|APE} = \frac{\overline{D}_{APE}}{\overline{D}_{APE} + \overline{\mathcal{E}}} \quad , \quad (21)$$

420 We can also assess irreversible mixing efficiency with the entropy production constituents
421 via

$$\gamma_S = \frac{\int \langle \chi/T^2 \rangle dt}{\int \langle \epsilon/T \rangle dt} \quad \text{and} \quad R_{f|S} = \frac{\int \langle \chi/T^2 \rangle dt}{\Delta S} \quad . \quad (22)$$

422 These mixing assessments and their input parameters are shown together in Table 1 as
423 an event summary for both cases.

424 The resulting mixing efficiency parameters demonstrate both increased energetic
425 extraction and reduced efficiency of extraction where T&K dynamics occur. The most
426 direct efficiency assessment yields $\gamma_E \approx 0.3$ for both DNS, consistent with the typical
427 range of $\gamma_E = 0.2 - 0.3$ seen in atmospheric and oceanic observations (see e.g., Gregg
428 et al., 2018; Lozovatsky & Fernando, 2013, and citations therein). The T&K-allowing
429 DNS generates 10% more PE than the T&K-prohibiting DNS in its final state, but it
430 does so with 7% lower γ_E due to its 19% larger ΔKE . The flux-based $\gamma_{\mathcal{W}}$ and ΔKE
431 partition-based γ_{KE} indicate a higher mixing efficiency of 0.5-0.63, with $R_{f|\mathcal{W}}$ and $R_{f|KE}$
432 values of 0.33-0.39 closer to γ_E . The inclusion of \mathcal{W}_{pv} in γ_{KE} and $R_{f|KE}$ yields mild ef-
433 ficiency reductions in the T&K-prohibiting case owing to net negative \mathcal{W}_{pv} work, which
434 increases the assessed available flux energy when compressible effects are considered. The
435 21-27% reduced $\gamma_{\{\mathcal{W}, KE\}}$ and 12-14% reduced $R_{f|\{\mathcal{W}, KE\}}$ in the T&K-allowing DNS stem
436 from 26-33% larger extractions of \mathcal{E} and $KE \rightarrow IE$ with only slightly (4%) larger $\int \mathcal{W}_b$.
437 The dissipation based metrics γ_{APE} and $R_{f|APE}$ and entropy-based metrics γ_S and $R_{f|S}$
438 have comparable efficiency ranges ($\gamma \approx 0.5-0.7$, $R_f \approx 0.3-0.4$) to the flux and KE partition-
439 based metrics, with the T&K-prohibiting case having slightly higher γ_{APE} and slightly
440 lower γ_S . As with the other efficiency metrics, the 16-27% lower $\gamma_{\{APE, S\}}$ and 11-18%
441 lower $R_{f|\{APE, S\}}$ in the T&K-allowing event suggest weaker mixing despite having 18%

Table 1. Event Mixing Efficiency Parameters

Parameter	Unit	T&K Prohibited	T&K Allowed	% Change ^a
ΔPE	J m^{-3}	9.21×10^{-5}	1.02×10^{-4}	+10.43%
ΔKE	J m^{-3}	-3.17×10^{-4}	-3.75×10^{-4}	+18.50%
γ_E	—	0.29	0.27	-6.81%
$\int \mathcal{W}_b dt$	J m^{-3}	1.15×10^{-4}	1.20×10^{-4}	+4.20%
$\int \mathcal{E} dt$	J m^{-3}	1.82×10^{-4}	2.41×10^{-4}	+32.60%
$\gamma_{\mathcal{W}}$	—	0.63	0.50	-21.42%
$R_{f \mathcal{W}}$	—	0.39	0.33	-14.29%
$\int (\mathcal{E} - \mathcal{W}_{pv}) dt$	J m^{-3}	1.90×10^{-4}	2.39×10^{-4}	+26.00%
γ_{KE}	—	0.61	0.50	-27.30%
$R_{f KE}$	—	0.38	0.33	-11.52%
\overline{D}_{APE}	W m^{-3}	3.45×10^{-8}	4.08×10^{-8}	+18.27%
$\overline{\mathcal{E}}$	W m^{-3}	5.13×10^{-8}	8.33×10^{-8}	+62.40%
γ_{APE}	—	0.67	0.49	-27.17%
$R_{f APE}$	—	0.40	0.33	-18.23%
$\int \langle \chi / T^2 \rangle dt$	$\text{J m}^{-3} \text{K}^{-1}$	4.28×10^{-7}	5.38×10^{-7}	+11.61%
$\int \langle \epsilon / T \rangle dt$	$\text{J m}^{-3} \text{K}^{-1}$	8.73×10^{-7}	1.16×10^{-6}	+32.62%
γ_S	—	0.55	0.46	-15.84%
$R_{f S}$	—	0.36	0.32	-10.82%

^aCalculated with respect to the T&K Prohibited value as 100%.

442 greater \overline{D}_{APE} and 12% greater $\int \langle \chi / T^2 \rangle$. These varied mixing efficiency assessments
 443 ultimately fail to capture the heightened energetic exchange, dissipation, and entropy
 444 production occurring in T&K events.

445 A more suitable mixing efficiency comparison between the two cases can be con-
 446 structed by isolating the reversible components of their net energy exchange terms. Fig-
 447 ure 10 shows the total $KE \rightleftharpoons IE$ and $KE \rightleftharpoons PE$ energy transfers for both cases
 448 decomposed into positive ($KE \Rightarrow$) and negative ($KE \Leftarrow$) components of integrated
 449 $(\mathcal{E} - \mathcal{W}_{pv})$ and \mathcal{W}_b . Since both transfers are net positive, the cancelled-out negative en-
 450 ergy transfer indicates how much of the positive energy transfer is reversed in the final
 451 state and can be assessed as a mixing inefficiency. In $KE \rightleftharpoons PE$, $KE \Leftarrow PE$ repre-
 452 sents vertically displaced particles returning from their displaced altitude rather than
 453 dissipating. In $KE \rightleftharpoons IE$, $KE \Leftarrow IE$, represents compressed regions adjacent to the
 454 expanding billows returning to their original pressure and volume as the KHI dissipate
 455 and mix with the surrounding fluid. These components reveal vastly larger reversed (i.e.
 456 wasted) energy transfers in the T&K-prohibiting DNS, where 44% of $KE \rightarrow IE$ is re-
 457 versed (vs. 16%) and 63% of $KE \rightarrow PE$ is reversed (vs. 10%). As a mixing efficiency
 458 metric, the amount of retained energy transfer can be expressed as

$$\gamma_{\{IE, PE\}} = \frac{KE \Rightarrow \{IE, PE\}}{KE \rightarrow \{IE, PE\}} \quad \text{and} \quad R_{f|\{IE, PE\}} = \frac{KE \Rightarrow \{IE, PE\}}{KE \rightarrow \{IE, PE\} - KE \Leftarrow \{IE, PE\}}, \quad (23)$$

459 where the values for the T&K-prohibiting (allowing) DNS are $\gamma_{IE} = 0.56$ (0.84, +50%),
 460 $R_{f|IE} = 0.39$ (0.73, +87%), $\gamma_{PE} = 0.37$ (0.90, +143%), and $R_{f|PE} = 0.22$ (0.81, +268%).

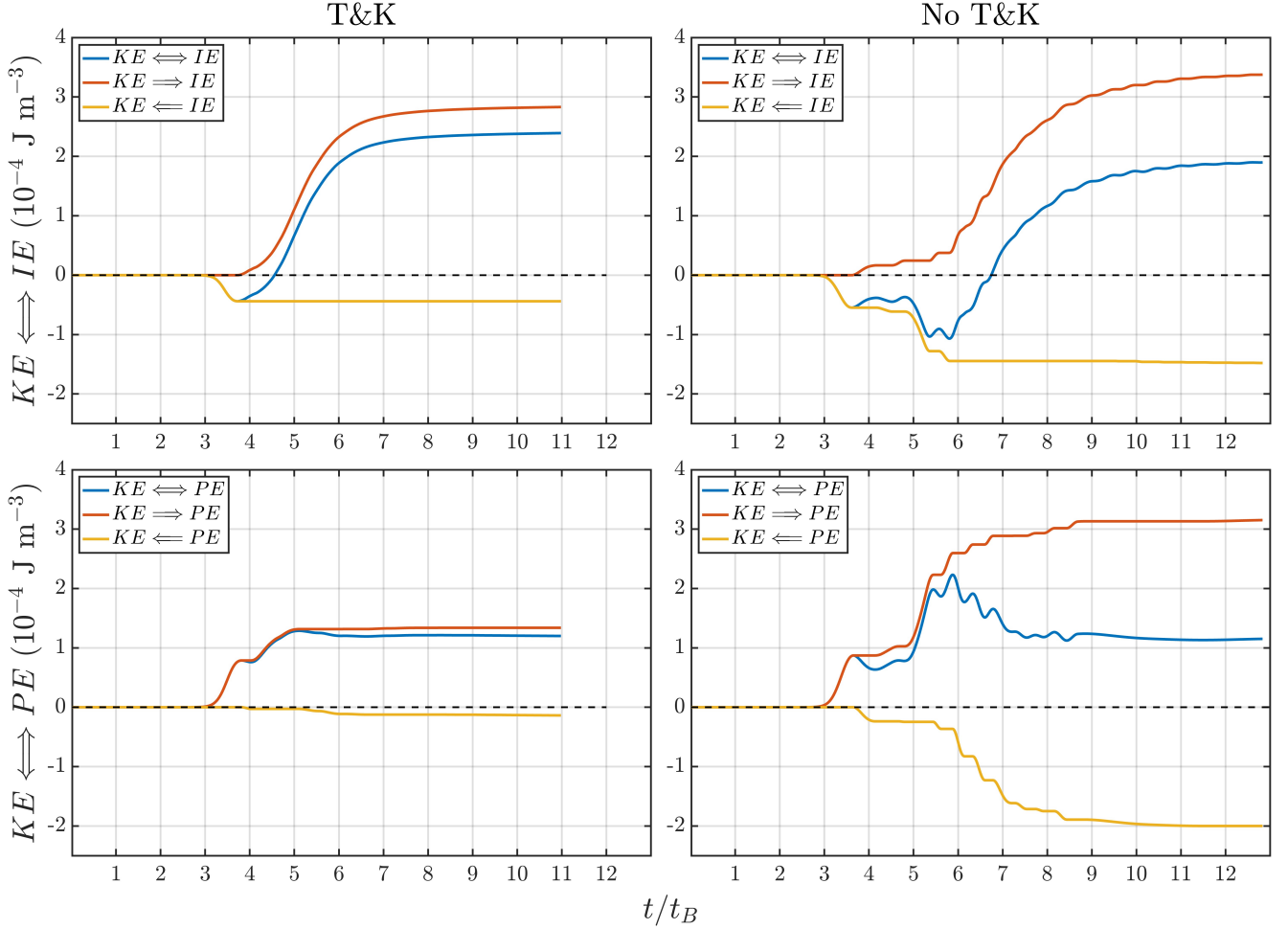


Figure 10. Comparing total (\Leftrightarrow), positive (\Rightarrow), and negative (\Leftarrow) components of integrated energy transfer from KE with and without T&K.

461 4 Summary and Conclusions

462 DNS presented in this study evaluate the impact of T&K dynamics on a thermo-
 463 spheric KHI event observed on 26 January 2018 over Poker Flats, Alaska. The instabil-
 464 ity event was triggered by elevated shear and temperature perturbations from a local 4
 465 km λ_z shear/stability enhancement superposed on a 16 km λ_z background IGW. Initial
 466 conditions generated from available observations reproduced the underlying 800 m layer
 467 having $Ri_{\min} = 0.05$ and $Re = 2200$. Identically initialized DNS were conducted in
 468 two spanwise box sizes to assess the instability and mixing consequences when KHI are
 469 not constrained to axial uniformity as in prior studies.

470 DNS allowing T&K dynamics reveal unique instability pathways that evolve faster
 471 turbulence transitions and yield more vigorous dissipation and mixing than morpholo-
 472 gies evolving from axially uniform KHI. Spanwise-billow distortions and misaligned bil-
 473 low junctions seed superpositions of billow linking vortex tubes and billow merging vor-
 474 tex knots consistent with morphologies identified by (Fritts, Wang, Lund, & Thorpe, 2022;
 475 Fritts, Wang, Thorpe, & Lund, 2022). These superposed T&K features develop mode
 476 1 and mode 2 twist wave evolutions that fragment their parent features into smaller in-
 477 tertwined vortex filaments with further elevated magnitudes. This rapid progression to

478 small scales stemming from initial T&K sites yields expanding turbulence regions that
479 quickly engulf the entire horizontal extent of the shear layer.

480 Cross-section comparisons with axially uniform KHI show T&K dynamics having
481 faster fine-scale evolution and locally larger dissipation. Faster turbulence pre-
482 cludes the development of billow merging and secondary CI/KHI, dominant evolutions
483 in the T&K-prohibiting case and previously thought to ubiquitously drive the turbulent
484 transition in all stratified shear turbulence scenarios. In the absence of T&K, weaker tur-
485 bulence damps dissipation as fluid parcels are repeatedly stirred about the billow core
486 rather than mixed.

487 The resulting macro-scale dissipation and energy exchanges conclusively quantify
488 the capacity for T&K instability events to contribute to elevated mixing in the thermo-
489 sphere and beyond, with far-reaching implications. T&K dynamics produce 94% (44%)
490 larger peak \mathcal{E} (\mathcal{X}) values $1.8 t_B$ ($1.2 t_B$) faster than axially uniform KHI. Billow pair-
491 ing and slowly evolving secondary CI/KHI in the T&K-prohibiting DNS yield oscillat-
492 ing \mathcal{W}_b and weaker, stepped evolutions of \mathcal{E} and \mathcal{X} . Over the whole event, T&K dynam-
493 ics accumulate 19% more ΔKE , 33% more \mathcal{E} , 26% more $KE \rightleftharpoons IE$, 62% more $\bar{\mathcal{E}}$, and
494 30% more ΔS than the T&K-prohibiting DNS, but they only yield 10% more ΔPE , 4%
495 more $KE \rightleftharpoons PE$, 18% more \bar{D}_{APE} , and 12% more \mathcal{X} . Consequently, γ and R_f values
496 are 7–27% smaller and 11–18% smaller, respectively, in the T&K-allowing DNS de-
497 spite displaying more mixing in every assessed standard metric. However, it is notewor-
498 thy that the T&K-allowing DNS retains a much greater fraction of its reversible energy
499 exchanges (50% greater γ_{IE} , 143% greater γ_{PE}), suggesting that other mixing metrics
500 may be valuable for assessing the relative impact of different instability dynamics in the
501 same environment.

502 The results of this study demonstrate that T&K dynamics dominate the turbulent
503 transition, extracting more energy and entropy more quickly from an existing background
504 environment than idealized, axially uniform KHI. T&K-induced twist waves, not secondary
505 CI/KHI, are shown to be the primary drivers of turbulence and dissipation in atmospheric
506 shear-driven flows. As such, studies of artificially constrained, axially uniform KHI in
507 narrow spanwise lab and simulation experiments severely underestimate the mixing im-
508 plications of KHI and inflate the importance of secondary CI/KHI and billow pairing
509 in atmospheric and oceanic flows. T&K events produce stronger mixing than axially uni-
510 form KHI but do so with reduced efficiency, converting a lower fraction (but larger net
511 amount) of the available kinetic energy into potential energy. Standard mixing efficiency
512 metrics do not capture the enhanced irreversible mixing of T&K events, suggesting that
513 more evaluation is needed of prevailing mixing metrics and available energy concepts to
514 capture T&K impacts in GCM turbulence parameterizations.

515 5 Open Research

516 The full domain 3-D data sets used in this study are too large to download from
517 the DoD HPCMP centers, but the datasets and associated scripts used to generate the
518 figures in this paper are publicly available online in the Figshare Data Repository via
519 <https://doi.org/10.6084/m9.figshare.22814600.v1>.

520 Acknowledgments

521 Research described here was supported by MURI Grant FA9550-18-1-0009 and NSF Grant
522 AGS-2230482. Poker Flats lidar data was provided by Bifford Williams. We also acknowl-
523 edge the support of the DoD High Performance Computing Modernization Program (HPCMP)
524 for access to several supercomputer platforms that enabled the simulations reported here.

525

References

526

Barat, J. (1982). Some characteristics of clear-air turbulence in the middle stratosphere. *Journal of Atmospheric Sciences*, *39*(11), 2553–2564.

527

528

Caulfield, C. P., & Kerswell, R. R. (2000). The nonlinear development of three-dimensional disturbances at hyperbolic stagnation points: A model of the braid region in mixing layers. *Physics of Fluids*, *12*(5), 1032–1043. doi: 10.1063/1.870358

531

532

Doddi, A., Lawrence, D., Fritts, D., Wang, L., Lund, T., Brown, W., . . . Kantha, L. (2021). Instabilities, dynamics, and energetics accompanying atmospheric layering (ideal) campaign: High-resolution in situ observations above the nocturnal boundary layer. *Atmospheric Measurement Techniques Discussions*, 1–33.

535

536

537

Felten, F. N., & Lund, T. S. (2006). Kinetic energy conservation issues associated with the collocated mesh scheme for incompressible flow. *J. Comp. Physics*, *215*, 465–484. doi: 10.1016/j.jcp.2005.11.009

538

539

Fritts, D. C., Baumgarten, G., Wan, K., Werne, J. A., & Lund, T. S. (2014). Quantifying kelvin-helmholtz instability dynamics observed in noctilucent clouds: 2. modeling and interpretation of observations. *Journal of Geophysical Research: Atmospheres*, *119*, 9359–9375. doi: 10.1002/2014JD021833

542

543

Fritts, D. C., & Dunkerton, T. J. (1985). Fluxes of heat and constituents due to convectively unstable gravity waves. *Journal of Atmospheric Sciences*, *42*(6), 549–556.

544

545

546

Fritts, D. C., Lund, A. C., Lund, T. S., & Yudin, V. (2022). Impacts of limited model resolution on the representation of mountain wave and secondary gravity wave dynamics in local and global models. 1: Mountain waves in the stratosphere and mesosphere. *Journal of Geophysical Research: Atmospheres*, *127*(9), e2021JD035990.

547

548

549

Fritts, D. C., & Wang, L. (2013). Gravity wave–fine structure interactions. part ii: Energy dissipation evolutions, statistics, and implications. *Journal of the Atmospheric Sciences*, *70*, 3735–3755. Retrieved from <http://journals.ametsoc.org/doi/abs/10.1175/JAS-D-13-059.1> doi: 10.1175/JAS-D-13-059.1

552

553

554

Fritts, D. C., Wang, L., Baumgarten, G., Miller, A. D., Geller, M. A., Jones, G., . . . Vinokurov, J. (2017). High-resolution observations and modeling of turbulence sources, structures, and intensities in the upper mesosphere. *Journal of Atmospheric and Solar-Terrestrial Physics*, 1–22. Retrieved from <http://linkinghub.elsevier.com/retrieve/pii/S1364682616304126> doi: 10.1016/j.jastp.2016.11.006

555

556

557

Fritts, D. C., Wang, L., Lund, T., & Thorpe, S. (2022). Multi-scale dynamics of kelvin-helmholtz instabilities. part 1. secondary instabilities and the dynamics of tubes and knots. *Journal of Fluid Mechanics*, *941*, A30.

562

563

564

Fritts, D. C., Wang, L., Thorpe, S., & Lund, T. (2022). Multi-scale dynamics of kelvin-helmholtz instabilities. part 2. energy dissipation rates, evolutions and statistics. *Journal of Fluid Mechanics*, *941*, A31.

565

566

567

Fritts, D. C., Wang, L., & Werne, J. A. (2013). Gravity wave–fine structure interactions. part i: Influences of fine structure form and orientation on flow evolution and instability. *Journal of the Atmospheric Sciences*, *70*, 3710–3734. doi: 10.1175/jas-d-13-055.1

568

569

570

Fritts, D. C., Wieland, S. A., Lund, T. S., Thorpe, S. A., & Hecht, J. H. (2021a). Kelvin-helmholtz billow interactions and instabilities in the mesosphere over the andes lidar observatory: 2. modeling and interpretation. *J. Geophys. Res. Atmos.*, *126*. doi: 10.1029/2020JD033412

571

572

573

Garcia, R. R., López-Puertas, M., Funke, B., Marsh, D. R., Kinnison, D. E., Smith, A. K., & González-Galindo, F. (2014, 5). On the distribution of co₂ and co in the mesosphere and lower thermosphere. *Journal of Geophysical Research*, *119*, 5700–5718. doi: 10.1002/2013JD021208

574

575

576

577

578

- 580 Garcia, R. R., Marsh, D. R., Kinnison, D. E., Boville, B. A., & Sassi, F. (2007, 5).
 581 Simulation of secular trends in the middle atmosphere, 1950-2003. *Journal of*
 582 *Geophysical Research Atmospheres*, *112*. doi: 10.1029/2006JD007485
- 583 Gardner, C. S. (2018, 6). Role of wave-induced diffusion and energy flux in
 584 the vertical transport of atmospheric constituents in the mesopause re-
 585 gion. *Journal of Geophysical Research: Atmospheres*, *123*, 6581-6604. doi:
 586 10.1029/2018JD028359
- 587 Gregg, M. C., D'Asaro, E. A., Riley, J. J., & Kunze, E. (2018). Mixing efficiency
 588 in the ocean. *Annual Review of Marine Science*, *10*(September 2017), 443-473.
 589 doi: 10.1146/annurev-marine-121916-063643
- 590 Hecht, J. H., Fritts, D. C., Gelinas, L. J., Rudy, R. J., Walterscheid, R. L., & Liu,
 591 A. Z. (2021). Kelvin-helmholtz billow interactions and instabilities in the
 592 mesosphere over the andes lidar observatory: 1. observations. *Journal of Geo-*
 593 *physical Research: Atmospheres*, *126*. doi: 10.1029/2020JD033414
- 594 Jeong, J., & Hussain, F. (1995). On the identification of a vortex. *J. Fluid Mech.*,
 595 *285*, 69-94.
- 596 Kantha, L., Lawrence, D., Luce, H., Hashiguchi, H., Tsuda, T., Wilson, R., ...
 597 Yabuki, M. (2017). Shigaraki uav-radar experiment (shurex): overview of
 598 the campaign with some preliminary results. *Progress in Earth and Planetary*
 599 *Science*, *4*(1), 1-26.
- 600 Kelvin, W. (1880). (1880), vibrations of a columnar vortex. *Phil. Mag.*, *10*, 155-
 601 168.
- 602 Klaassen, G., & Peltier, W. (1985). The onset of turbulence in finite-amplitude
 603 kelvin-helmholtz billows. *Journal of Fluid Mechanics*, *155*, 1-35.
- 604 Lehmacher, G., Scott, T., Larsen, M., Bilén, S., Croskey, C., Mitchell, J., ... Collins,
 605 R. (2011). The turbopause experiment: atmospheric stability and turbulent
 606 structure spanning the turbopause altitude. In *Annales geophysicae* (Vol. 29,
 607 pp. 2327-2339).
- 608 Liu, H. L. (2000, may). Temperature changes due to gravity wave saturation.
 609 *Journal of Geophysical Research Atmospheres*, *105*(D10), 12329-12336. doi:
 610 10.1029/2000JD900054
- 611 Liu, H. L. (2021). Effective vertical diffusion by atmospheric gravity waves. *Geo-*
 612 *physical Research Letters*, *48*, 1-10. doi: 10.1029/2020GL091474
- 613 Lozovatsky, I., & Fernando, H. (2013). Mixing efficiency in natural flows. *Philo-*
 614 *sophical Transactions of the Royal Society A: Mathematical, Physical and*
 615 *Engineering Sciences*, *371*(1982), 20120213.
- 616 McIntyre, M. E. (1989). On dynamics and transport near the polar mesopause
 617 in summer. *Journal of Geophysical Research: Atmospheres*, *94*(D12), 14617-
 618 14628.
- 619 Mesquita, R. L., Larsen, M. F., Azeem, I., Stevens, M. H., Williams, B. P., Collins,
 620 R. L., & Li, J. (2020). In situ observations of neutral shear instability in
 621 the statically stable high-latitude mesosphere and lower thermosphere during
 622 quiet geomagnetic conditions. *Journal of Geophysical Research: Space Physics*,
 623 *125*, 1-14. Retrieved from <https://doi.org/10.1029/2020JA027972> doi:
 624 10.1029/2020JA027972
- 625 Moin, P., & Mahesh, K. (1998). Direct numerical simulation: A tool in turbulence
 626 research. *Annual Review of Fluid Mechanics*, *30*(539), 78-xx.
- 627 Osborn, T. (1980). Estimates of the local rate of vertical diffusion from dissipation
 628 measurements. *Journal of physical oceanography*, *10*(1), 83-89.
- 629 Osborn, T. R., & Cox, C. S. (1972). Oceanic fine structure. *Geophysical Fluid Dy-*
 630 *namics*, *3*(4), 321-345.
- 631 Peltier, W., & Caulfield, C. (2003). Mixing efficiency in stratified shear flows. *An-*
 632 *nuual review of fluid mechanics*, *35*(1), 135-167.
- 633 Pope, S. B. (2000). *Turbulent flows* (Vol. 1). Cambridge University Press. doi: 10
 634 .1017/CBO9780511840531

- 635 Sato, T., & Woodman, R. F. (1982). Fine altitude resolution observations of strato-
636 spheric turbulent layers by the arecibo 430 mhz radar. *Journal of Atmospheric*
637 *Sciences*, *39*(11), 2546–2552.
- 638 Swenson, G., Yee, Y., Vargas, F., & Liu, A. (2018, 10). Vertical diffusion transport
639 of atomic oxygen in the mesopause region consistent with chemical losses and
640 continuity: Global mean and inter-annual variability. *Journal of Atmospheric*
641 *and Solar-Terrestrial Physics*, *178*, 47-57. doi: 10.1016/j.jastp.2018.05.014
- 642 Tailleux, R. (2009). On the energetics of stratified turbulent mixing, irreversible
643 thermodynamics, Boussinesq models and the ocean heat engine controversy.
644 *Journal of Fluid Mechanics*, *638*, 339–382. doi: 10.1017/S002211200999111X
- 645 Tailleux, R. (2013). Irreversible compressible work and available potential energy
646 dissipation in turbulent stratified fluids. *Physica Scripta*, *88*(T155). doi: 10
647 .1088/0031-8949/2013/T155/014033
- 648 Thorpe, S. A. (1987). Transitional phenomena and the development of turbulence in
649 stratified fluids: a review. *J. Geophys. Res.*, *92*, 5231–5248.
- 650 Weinstock, J. (1978). Vertical turbulent diffusion in a stably stratified fluid. *Journal*
651 *of Atmospheric Sciences*, *35*(6), 1022–1027.
- 652 White, F. M. (1974). *Viscous fluid flow*. McGraw-Hill, New York.
- 653 Winters, K. B., Lombard, P. N., Riley, J. J., & D’Asaro, E. A. (1995). Available po-
654 tential energy and mixing in density-stratified fluids. *Journal of Fluid Mechan-*
655 *ics*, *289*, 115–128.